

# Hybrid Emission Modeling of GRB 221009A: Shedding Light on TeV Emission Origins in Long-GRBs

HEBZIBHA ISRAVEL <sup>1</sup>, DAMIEN BÉGUÉ <sup>2</sup>, AND ASAF PE'ER <sup>2</sup>

<sup>1</sup>*Ben-Gurion University of the Negev  
Beer-Sheva 8410501, Israel*  
<sup>2</sup>*Bar-Ilan University  
Ramat-Gan 5290002, Israel*

## ABSTRACT

Observations of long duration gamma-ray bursts (GRBs) with TeV emission during their afterglow have been on the rise. Recently, GRB 221009A, the most energetic GRB ever observed, was detected by the LHAASO experiment in the energy band 0.2 - 7 TeV. Here, we interpret its afterglow in the context of a hybrid model in which the TeV spectral component is explained by the proton-synchrotron process while the low energy emission from optical to X-ray is due to synchrotron radiation from electrons. We constrained the model parameters using the observed optical, X-ray and TeV data. By comparing the parameters of this burst and of GRB 190114C, we deduce that the VHE emission at energies  $\geq 1$  TeV in the GRB afterglow requires large explosion kinetic energy,  $E \gtrsim 10^{54}$  erg and a reasonable circumburst density,  $n \gtrsim 10$  cm<sup>-3</sup>. This results in a small injection fractions of particles accelerated to a power-law,  $\sim 10^{-2}$ . A significant fraction of shock energy must be allocated to a near equipartition magnetic field,  $\epsilon_B \sim 10^{-1}$ , while electrons should only carry a small fraction of this energy,  $\epsilon_e \sim 10^{-3}$ . Under these conditions required for a proton synchrotron model, namely  $\epsilon_B \gg \epsilon_e$ , the SSC component is substantially sub-dominant over proton-synchrotron as a source of TeV photons. These results lead us to suggest that proton-synchrotron process is a strong contender for the radiative mechanisms explaining GRB afterglows in the TeV band.

*Keywords:* Gamma-ray bursts(629) — Synchrotron emission(856) — Gamma-ray transient sources(1853) — source : GRB 221009A — GRB 190114C — particle acceleration

## 1. INTRODUCTION

Gamma Ray Bursts (GRB) are indisputably the universe's brightest extragalactic transient events. They feature a brief prompt phase emission, mostly observed in the energy extending from a few keVs to a few GeVs. It is then followed by the extended broadband afterglow, detected at all energy bands, from radio to a few hundreds of GeVs and possibly even higher (for reviews see *e.g.* Piran 1999; Mészáros 2006; Kumar & Zhang 2015; Zhang 2018). Detections of GRB afterglows at the highest energies (*i.e.*,  $> 300$  GeV) have been on the rise in the past two decades (for reviews, see, *e.g.*, Nava 2018; Miceli & Nava 2022). Understanding the physics underlying this emission has become of highest importance as it holds the clues to better constrain and understand the afterglow of GRBs.

The recent development of highly sensitive ground-based detectors, such as the High Energy Stereoscopic System (H.E.S.S., Aharonian et al. 1997; H. E. S. S. Collaboration et al. 2021), the Major Atmospheric Gamma Imaging Cherenkov (MAGIC, Lorenz 2005), and the more recent Large High Altitude Air Shower Observatory (LHAASO, Cao et al. 2019), has allowed for the detection of sub-TeV to  $\sim$  TeV signal in GRBs and measurements of their spectra in this band. Examples include GRB 180720B (Abdalla et al. 2019), GRB 190114C (Acciari et al. 2019a), GRB 190829A (H. E. S. S. Collaboration et al. 2021) and GRB 201216C (Blanch et al. 2020).

The emission mechanism of GRBs with emission at the very high energy (VHE,  $\geq$  TeV) band is highly debated. With reference to the fireball scenario, the synchrotron self-Compton (SSC) model is prominent among the radiation mechanisms that aim to explain these signals. In this mechanism, photons emitted by the synchrotron process at low energies, are upscattered to VHE by the energetic electrons that emitted them (Ghisellini & Celotti 1998; Dermer et al. 2000; Sari & Esin 2001; Fraija et al. 2019; Wang et al. 2019; Derishev & Piran 2021a; Fraija et al. 2022; Yamasaki

& Piran 2022). Alternatively, the proton-synchrotron mechanism has been suggested to produce a photon signal at these extreme energies (Vietri 1997; Böttcher & Dermer 1998; Isravel et al. 2022; Zhang et al. 2022). The idea is that the same mechanism responsible for accelerating electrons also accelerates protons to high energies. The energetic protons then emit the observed VHE photons, reaching energies as high as  $\gtrsim$  TeV (Totani 1998; Zhang & Mészáros 2001; Isravel et al. 2022). In addition, photo-pion and photo-pair production processes may also produce VHE photons (see e.g. Razzaque et al. 2010) although this requires a compact region, and it is not clear how this is obtained at late times.

The recent detection of TeV photons from GRB 221009A allows for the first time to probe in great details the GRB afterglow phase in this energy band. This GRB is by far the brightest GRB ever detected (Lesage et al. 2023). It was observed at the energy band 0.2 - 7 TeV by LHAASO (LHAASO-Collaboration et al. 2023). The isotropic equivalent luminosity in the band 0.3 – 5 TeV is  $7.3 \times 10^{50}$  erg s<sup>-1</sup> and the observed peak flux is  $\sim 1.2 \times 10^{-5}$  erg cm<sup>-2</sup> s<sup>-1</sup> (LHAASO-Collaboration et al. 2023). This GRB is a nearby burst, at a cosmological redshift  $z = 0.151$  (de Ugarte Postigo A. et al. 2022; Castro-Tirado et al. 2022) as well as the brightest burst ever detected, with an isotropic equivalent burst energy  $E_{iso} \simeq 3 \times 10^{54}$  erg (Frederiks et al. 2022). The half opening angle of the jet is estimated to be  $\sim 0.8^\circ$  (LHAASO-Collaboration et al. 2023).

Several authors considered the conventional SSC model to interpret the VHE afterglow spectrum of GRB 221009A. This process is a natural outcome of the classical synchrotron-SSC emission model, and can account for emission in this energy band. However, it is not clear yet whether this model can explain the broad-band data (at all wavelengths), given the strong constraints on the TeV band flux from radio, optical and X-ray data (González et al. 2022; Miceli & Nava 2022). Furthermore, this model cannot explain a  $\gtrsim 10$  TeV energy photons (Huang, Y. 2022) originally claimed to be observed (González et al. 2022; Ren et al. 2022; Kann et al. 2023; Das & Razzaque 2023; Laskar et al. 2023a). On the other hand, it is not clear if photons at these energies were detected<sup>1</sup> and required to explain the observed spectra (LHAASO-Collaboration et al. 2023). A recent work by Zhang et al. (2022) considered the possibility that proton-synchrotron may be the source of  $\gtrsim$  TeV energy photons in the reverse shock scenario, and concluded that this is a plausible scenario under certain conditions, in particular a very strong magnetic field.

Here, we use the data available from optical through X-rays to TeV, and show that the synchrotron emission from relativistic protons can explain both the flux and the temporal features of the VHE afterglow of GRB 221009A, while its lower-energy afterglow counterpart is interpreted with the electron-synchrotron process. We determined two sets of parameters able to explain the observational features of this burst. Then by comparing these model parameters with those deduced for GRB 190114C (Isravel et al. 2022), we identify a set of consistent characteristics for the VHE afterglows with energies  $\gtrsim$  TeV, within the framework of the hybrid model we present.

This paper is structured as follows. In section 2 we review the available data on GRB 221009A obtained by various space-based and ground-based facilities. In section 3, we present our model within the context of the standard fireball scenario. We then use the data to constrain the values of the free physical parameters in section 4. The SEDs are then produced for three different cases in section 5. We investigate the common features encountered in the VHE afterglows of GRBs in section 6. Finally, our conclusions follow in section 7.

## 2. OBSERVATIONAL DATA OF GRB 221009A

The long-duration GRB 221009A triggered the Gamma-Ray Burst Monitor (GBM) on board the *Fermi* spacecraft on October 9, 2022, at  $T_0 =$  UT 13:16:59 (Veres et al. 2022). Initially, the GBM captured two separate emission episodes (Lesage et al. 2022). The first occurred between  $T_0-0$  and  $T_0+43.4$  s with a reported peak energy of  $375 \pm 87$  keV and a fluence of  $2.12 \pm 0.05 \times 10^{-5}$  erg cm<sup>-2</sup> in the energy range 10-1000 keV. The second episode, being the brightest, exhibited numerous peaks during the time interval  $T_0+175$  to  $T_0+1458$  s. Due to the saturation of the detectors caused by the accumulation of photons in several of these peaks, the exact flux can hardly be measured. Yet, the KONUS-WIND collaboration recently reported the fluence  $\sim 0.21$  erg cm<sup>-2</sup> within the energy band 20 keV - 10 MeV (Frederiks et al. 2023).

The High Energy (HE) X-ray telescope on board the *Insight*-Hard X-ray Modulation Telescope (*Insight*-HXMT) also triggered and monitored this burst on 9<sup>th</sup> October 2022, at 13:17:00.050 UT (Tan et al. 2022). This instrument's primary goal is to observe GRBs and electromagnetic counterparts of gravitational waves (Cai et al. 2021). The *Insight*-HXMT together with the Gravitational Wave High-energy Electromagnetic Counterpart All-sky Monitor (GECAM-C)

<sup>1</sup> In their analysis, the LHAASO collaboration cut the spectrum at 7 TeV.

measured the emission in the energy band  $\sim 10$  KeV to 6 MeV starting from the precursor of the event until the early afterglow phase for a duration of about  $\sim 1800$  s (An et al. 2023). It was determined that the burst has a total isotropic energy of  $\approx 1.5 \times 10^{55}$  ergs.

The *Fermi*-Large Area Telescope (LAT) subsequently observed this GRB between 200 and 800 s following the GBM trigger (Pillera et al. 2022). It is the brightest GRB ever detected by LAT, with a maximum reported photon energy of 99.3 GeV, observed 240 s after  $T_0$ . Due to the extreme brightness, the *Fermi*-LAT detector was saturated during the time period 200-400 s (corresponding to "bad" time intervals, where the exact flux could not be measured due to the saturation; see Omodei, N. 2022a,b). The LAT data in the energy band 0.1 -1 GeV between 400 s and 800 s was modeled by a power-law spectrum  $dN/dE = N_0 (E_{LAT}/E_f)^{p_0}$  resulting in a spectral index  $p_0 = 1.87 \pm 0.04$  and in a photon flux of  $\Phi_\gamma = 6.2 \pm 0.4 \times 10^{-3}$  ph cm $^{-2}$  s $^{-1}$  (Pillera et al. 2022).

Nearly 53.3 minutes after the GBM trigger, at UT 14:10:17, the *Swift*-Burst Alert Telescope (BAT) also triggered and observed GRB 221009A in the hard X-ray band (Dichiara et al. 2022). Starting 143 s after the BAT trigger, *Swift*-XRT slewed and monitored the then steadily declining X-ray light curve with a photon index  $1.836 \pm 0.012$  and a temporal index of  $1.509 \pm 0.004$  (Evans et al. 2007, 2009).

The optical afterglow in the R-band was measured at 18:45 UT, 4.6 hours after the BAT trigger, corresponding to 5.5 hours after the GBM trigger, with magnitude  $16.57 \pm 0.02$  by the Observatorio Sierra Nevada (OSN) in Spain (Hu et al. 2022). Considering the strong galactic extinction in the R-band, the AB magnitude is estimated to be 3.710 (Schlegel et al. 1998). The optical and infrared data between 0.2 and 0.5 days are presented in O'Connor et al. (2023) and Gill & Granot (2023), and are corrected for the galactic extinction of 1.32 mag. For instance, 179 s after the BAT trigger, *swift*-UVOT observed GRB 221009A and recorded a magnitude of  $16.68 \pm 0.03$  in the white filter (Kuin et al. 2022).

Finally, LHAASO's Water Cherenkov Detector Array (WCDA) (Cao et al. 2019) observed GRB 221009A within its field of view at the time of the GBM trigger. Within a span of 3000 s from the burst trigger, more than 60,000 photons in the energy band 0.2  $\sim$  7 TeV were detected by the LHAASO (LHAASO-Collaboration et al. 2023). Around the phase of the main burst, LHAASO recorded the flux of  $\sim 6 \times 10^{-8}$  erg cm $^{-2}$  s $^{-1}$  at 1 TeV at the time period between  $T_0 + 220$  s  $-$   $T_0 + 230$  s, after correcting for extra-galactic background light (EBL) attenuation<sup>2</sup>.

The LHAASO collaboration and the Fermi-GBM collaboration deduced different times for the onset of the afterglow. Lesage et al. (2023) for the Fermi-GBM collaboration argued that the beginning of the afterglow phase was  $\sim 597$  s after the trigger. This is based on the inability of a single decay function to explain the lightcurve at earlier times. On the other hand, interpretation of the LHAASO data in the framework of the external shock, based on the temporal decay of the light-curve lead to estimating the onset of the afterglow at this band already at 226 s after the GBM trigger (LHAASO-Collaboration et al. 2023). The origin of this discrepancy can be due to the superposition of both prompt signal (which should originate from a small radius) and afterglow signal (originating from a forward shock propagating ahead of the jet, at larger radius) in the observations around few hundreds seconds. Therefore, here we will model the LHAASO emission as part of the afterglow and will not attempt to model the GBM data, which, as we will show below, is much brighter than the predicted GBM flux within the framework of our model (assumed to be produced by electron-synchrotron in this energy band).

### 3. MODEL DESCRIPTION

In this section, we detail the afterglow dynamics and the emission mechanisms, which serve as the basis of our model attempting to explain the VHE observation of GRB 221009A. We set our analysis within the framework of the fireball evolution scenario (Paczynski 1990; Piran et al. 1993; Mészáros et al. 1998), further assuming that the high-energy component (GeV  $\lesssim$   $E_\gamma \leq$  TeV) and the low-energy component (eV  $\lesssim$   $E_\gamma \leq$  MeV) of the observed spectrum are produced by synchrotron radiation from the accelerated protons and electrons, respectively via the external shock acceleration. More details on the processes and the model can be found in Isravel et al. (2022), and we remind here only the key assumptions and equations.

When the relativistic jet originating from the compact GRB progenitor encounters the stationary ambient environment, an outward propagating shock-wave is created (Paczynski & Rhoads 1993; Medvedev & Loeb 1999). This shock collects and accelerates the ambient matter (both protons and electrons) and generates in-situ a magnetic field. The accelerated particles then produce the observed multi-wavelength emission (see *e.g.* Sari & Piran 1995; Sari et al.

<sup>2</sup> As the VHE photons traversing through cosmological sources experience  $\gamma\gamma$ -pair-production by interacting with the EBL, which substantially attenuates the intrinsic spectrum of the source (Ackermann et al. 2012).

1998; Panaitescu & Kumar 2000). During the afterglow phase, the emission occurs while the outflow expands in a self-similar way, following the Blandford & McKee (1976) solution. We assume here that the ultra-relativistic expansion can be considered adiabatic, *i.e.* that the radiative losses of the plasma behind the shock are negligible. This is a good approximation for our scenario as accelerated protons should carry most of the internal energy while they do not radiate efficiently.

Under those assumptions, the Lorentz factor of the jet, at a given observed time  $t$ , is determined only by the isotropic-equivalent explosion kinetic energy  $E$ , and the ambient ISM density  $n$ :

$$\Gamma(E, n; t) = \left[ \frac{17E(1+z)}{1024\pi n m_p c^5 t^3} \right]^{1/8} = 61.3 E_{54}^{1/8} n_0^{-1/8} t_3^{-3/8}, \quad (1)$$

where  $c$  is the speed of light,  $m_p$  is the mass of the proton and we took the redshift to be  $z = 0.151$  relevant for GRB 221009A. Here and below,  $Q = 10^x Q_x$  in cgs units is employed. Using  $t = r/(4\Gamma^2(r)c)$ , one can express the location of the blast wave as a function of the observed time,

$$r(E, n; t) = \left[ \frac{17Et}{4\pi n m_p c(1+z)} \right]^{1/4} = 3.9 \times 10^{17} E_{54}^{1/4} n_0^{-1/4} t_3^{1/4} \text{ cm}. \quad (2)$$

Finally, we define the comoving shock expansion (dynamical) time as  $t_{dyn} = r/(\Gamma c) = 2.1 \times 10^5 E_{54}^{1/8} t_3^{5/8} n_0^{-1/8}$  s.

In order to estimate the observed spectrum, we need to specify the magnetic field and the particle distribution functions. For the former, we take the standard assumption that an (uncertain) fraction,  $\epsilon_B$ , of the post-shock thermal energy is used in generating a magnetic field. This gives

$$B = \sqrt{32\pi\epsilon_B\Gamma^2 n m_p c^2} = 7.5 E_{54}^{1/8} \epsilon_{B,-1}^{1/2} n_0^{3/8} t_3^{-3/8} \text{ G}. \quad (3)$$

For the radiating particles, namely protons and electrons, we assume that a fraction  $\xi_x$  of all the particle is injected in the radiative zone with a power-law distribution between some minimum Lorentz factor  $\gamma_{m,i}$  and maximum Lorentz factor,  $\gamma_{\max,i}$ , such that they carry a fraction  $\epsilon_i$  of the available internal energy. The power-law index is referred to as  $p_i$ . Here, the subscript  $i$  refers either to electrons  $i = e$  or to protons  $i = p$ . Energetic consideration provides the constraint  $\epsilon_B + \epsilon_e + \epsilon_p < 1$ .

The minimum Lorentz factors of the protons and electrons are readily obtained as

$$\gamma_{m,p} \simeq 6 f_p \xi_p^{-1} E_{54}^{1/8} n_0^{-1/8} t_3^{-3/8} \epsilon_{p,-1}, \quad (4)$$

$$\gamma_{m,e} = 450 f_e \xi_e^{-1} E_{54}^{1/8} n_0^{-1/8} t_3^{-3/8} \epsilon_{e,-2}. \quad (5)$$

where  $f_i$  is a function of  $p_i$  and is equal to  $f_i = (p_i - 2)/(p_i - 1)$  for  $p_i > 2$  and  $f_i = \ln(\gamma_m/\gamma_{\max})$  for  $p_i = 2$  (Sari et al. 1998).

Another characteristic particle Lorentz factor is obtained by equating the synchrotron cooling time to the dynamical time, providing the cooling Lorentz factor of the particle. The synchrotron cooling time is given by  $t_{syn} = (6\pi m_i c)/(\gamma_i B^2 \sigma_{T,i})$ , where  $\sigma_{T,e}$  is the Thomson cross-section and  $\sigma_{T,p} = (m_e^2/m_p^2)\sigma_{T,e}$ . This gives  $\gamma_{c,i} = (6\pi m_i c)/(\sigma_{T,i} B^2 \Gamma t)$ , resulting in

$$\gamma_{c,e} = 222.3 t_3^{1/8} \epsilon_{B,-1}^{-1} E_{54}^{-3/8} n_0^{-5/8}, \quad (6)$$

$$\gamma_{c,p} = 1.4 \times 10^{12} t_3^{1/8} \epsilon_{B,-1}^{-1} E_{54}^{-3/8} n_0^{-5/8}. \quad (7)$$

A proton synchrotron model requires the magnetic field to be large, and therefore, from Equations (5) and (6), it follows that  $\gamma_{c,e} < \gamma_{m,e}$ , hence the electrons are in the fast cooling regime, and the electron distribution function is a broken power-law with index of 2 between  $\gamma_{c,e}$  and  $\gamma_{m,e}$ , and  $p_e - 1$  above  $\gamma_{m,e}$ . However from Equation (4), it is seen that  $\gamma_{m,p} \ll \gamma_{c,p}$ , meaning that the proton population is in the slow cooling regime.

The maximum Lorentz factor  $\gamma_{\max,i}$  of the accelerated particles is obtained by equating the acceleration time to the synchrotron cooling time. It comes

$$\gamma_{\max,i} = (6\pi q/\alpha\sigma_{T,i}B)^{1/2} \quad (8)$$

where the numerical coefficient  $\alpha$  prescribes the acceleration efficiency. The maximum Lorentz factor for protons is

$$\gamma_{\max,p} = 7.8 \times 10^{10} \alpha^{-1/2} E_{54}^{-1/16} n_0^{-3/16} t_3^{3/16} \epsilon_{B,-1}^{-1/4}. \quad (9)$$

Since  $\gamma_{\max,p} < \gamma_{c,p}$ , the proton distribution function is a single power-law above  $\gamma_{m,p}$  with an exponential cutoff at the very high energy end of the proton distribution spectrum, producing an exponential cut-off in the resulting photon spectrum. For electrons,  $\gamma_{\max,e}$  is  $m_p/m_e$  times smaller than  $\gamma_{\max,p}$ , but as the electron-synchrotron flux at such high energies is very small, we omit the discussion on it here.

Each of those characteristic Lorentz factors in the particle distribution functions is associated to a characteristic synchrotron frequency such that  $\nu = (3qB\gamma^2\Gamma)/(4\pi(1+z)m_i c)$ . At these frequencies, the observed synchrotron spectrum presents a spectral break. For the electrons, the observed spectrum is  $F_\nu \propto (\nu^{1/3}, \nu^{-1/2}, \nu^{-p_e/2})$  for ( $\nu < \nu_{c,e}$ ;  $\nu_{c,e} < \nu < \nu_{m,e}$ ;  $\nu_{m,e} < \nu$ ), where  $\nu$  is the observed frequency. The proton synchrotron spectrum is shaped as  $F_\nu \propto (\nu^{1/3}, \nu^{-(p_p-1)/2})$  for ( $\nu < \nu_{m,p}$ ;  $\nu_{m,p} < \nu < \nu_{\max,p}$ ).

The characteristic frequencies associated with particles at  $\gamma_m$  are given by

$$h\nu_{m,p} = 7.6 \times 10^{-9} f_p^2 E_{54}^{1/2} t_3^{-3/2} \epsilon_{B,-1}^{1/2} \epsilon_{p,-1}^2 \xi_p^{-2} \text{ eV}, \quad (10)$$

$$h\nu_{m,e} = 1.42 f_e^2 E_{54}^{1/2} t_3^{-3/2} \epsilon_{B,-1}^{1/2} \epsilon_{e,-2}^2 \xi_e^{-2} \text{ eV}. \quad (11)$$

The cooling frequency for the electrons is

$$h\nu_{c,e} = 0.35 E_{54}^{-1/2} t_3^{-1/2} \epsilon_{B,-1}^{-3/2} n_0^{-1} \text{ eV}, \quad (12)$$

and the maximum frequency for the protons reads

$$h\nu_{\max,p} \sim 23 \alpha^{-1} E_{54}^{1/8} n_0^{-1/8} t_3^{-3/8} \text{ TeV}. \quad (13)$$

Hence, the shock accelerated protons can emit synchrotron photons at energies as high as 10 TeV above those detected by LHAASO.

The spectral flux is calculated as follows. The maximum power emitted by a single particle via the synchrotron process at the observed peak frequency is  $P_{\nu_{\max}} = (2m_i c^2 \sigma_{T,i} B \Gamma / 9q)(1+z)$ . Assuming the total number of radiating particles to be  $N_i = 4\pi \xi_i n r^3 / 3$ , the peak flux associated with the electron synchrotron process is

$$F_{\nu_{\text{peak},e}} = \frac{N_e P_{\nu_{e,\max}}}{4\pi d_L^2} = 2.7 \times 10^{-21} \frac{\xi_e E_{54} \epsilon_{B,-1}^{1/2} n_0^{1/2}}{d_{L,27}^2} \text{ erg cm}^{-2} \text{ s}^{-1} \text{ Hz}^{-1}, \quad (14)$$

where we normalised the luminosity distance  $d_L$  to  $10^{27}$  cm, given the proximity of GRB 221009A at redshift  $z = 0.151$  (de Ugarte Postigo A. et al. 2022; Castro-Tirado et al. 2022) corresponding to  $d_L = 2.23 \times 10^{27}$  cm (assuming a flat  $\Lambda$ CDM cosmology with  $H_0 = 69.6 \text{ km s}^{-1} \text{ Mpc}^{-1}$ ,  $\Omega_M = 0.286$ , and  $\Omega_\Lambda = 0.714$ , Wright 2006). Since in our scenario the electrons are in the fast cooling regime, analysing the spectrum reveals that  $\nu_{c,e} < \nu_o < \nu_{m,e} < \nu_{XRT}$ , where  $\nu_{XRT} = 0.3 \text{ keV}$  is the low energy threshold of the XRT instrument and  $\nu_o \sim 1 \text{ eV}$  is the typical frequency of the optical band. The flux at frequencies lower than  $\nu_{m,e}$  and greater than  $\nu_{c,e}$  is given by

$$F_{\nu,e} = F_{\nu_{\text{peak},e}} (\nu/\nu_{c,e})^{-1/2}, \quad (15)$$

while the flux at frequencies higher than  $\nu_{m,e}$  is given by

$$F_{\nu,e} = F_{\nu_{\text{peak},e}} (\nu_{m,e}/\nu_{c,e})^{-1/2} (\nu/\nu_{m,e})^{-p_e/2}. \quad (16)$$

Similarly, the peak flux associated with the proton-synchrotron process is given by

$$F_{\nu_{\text{peak},p}} = \frac{N_p P_{\nu_{p,\max}}}{4\pi d_L^2} = 1.46 \times 10^{-24} \frac{\xi_p E_{54} \epsilon_{B,-1}^{1/2} n_0^{1/2}}{d_{L,27}^2} \text{ erg cm}^{-2} \text{ s}^{-1} \text{ Hz}^{-1}, \quad (17)$$

and the spectrum within the frequency range  $\nu_{m,p} \leq \nu \leq \nu_{\max,p}$  for the slow-cooling synchrotron process is a power-law

$$F_{\nu,p} = F_{\nu_{\text{peak},p}} (\nu/\nu_{m,p})^{-\frac{(p_p-1)}{2}}. \quad (18)$$



#### 4. LIMITATIONS ON THE MODEL PARAMETERS: AN ANALYTICAL APPROACH

The best fit to the temporal decay of the X-ray flux as observed by the *swift*-XRT consists of five breaks at times between  $T_0 + 3.27 \times 10^4$  s to  $T_0 + 4.5 \times 10^6$  s. The corresponding decay indices at the break times are presented in the XRT catalogue of the burst (Evans et al. 2009). At observed times  $t < 3 \times 10^4$  s, the decay index in the XRT band is identified to be  $\sim -3/2$ .<sup>3</sup> At later times, the lightcurve becomes steeper, and may be associated with a jet break. In order to reproduce the temporal decay in the XRT band with  $\nu_c < \nu_m < \nu_{XRT}$  (fast cooling regime, as required by the electron synchrotron model), the condition  $p_e \sim 8/3 \sim 2.67$  must be satisfied as  $F_\nu \propto t^{\frac{2-3p}{4}}$ .<sup>4</sup>

On the other hand, the TeV temporal decay is  $-1.115 \pm 0.012$  (LHAASO-Collaboration et al. 2023). This result is challenging for the SSC model, as it seem outside the expected temporal slope for electrons with a power law index of 2.67, which is  $-1.625$  (Sari & Esin 2001) in the fast cooling regime.<sup>5</sup> We can therefore exploit the proton-synchrotron model, with proton power law index of  $\approx 2.2 - 2.3$  in the slow cooling regime, as explained above. This is the index needed to explain the LHAASO data. In fact, setting  $p_e \equiv p_p \sim 8/3$  leads to an energy crisis, as the energy budget in the proton-synchrotron component will be very high. Therefore, in presenting our results for GRB 221009A, we will set a proton power law index  $p_p = 2.3$ , but allow for a different value of  $p_p = 2.2$  in interpreting the TeV data. We will keep the constraint  $p_e = 8/3$  in order to satisfy the XRT temporal decay.

##### 4.1. Constraints for a proton-synchrotron model

We use the observed flux of GRB 221009A to constrain the values of the free model parameters. We start with the flux at 1 TeV as observed by the LHAASO experiment at time  $t = 235$  s after the trigger. By equating the LHAASO reported flux  $[\nu F_\nu]_p \approx 2 \times 10^{-6}$  ergs cm<sup>-2</sup> s<sup>-1</sup> (LHAASO-Collaboration et al. 2023) and the expected proton-synchrotron flux given in Equation (18) at 1 TeV, the fractional energy of the magnetic field as a function of the other free parameters is,

$$\epsilon_{B,-1} = 0.1 \cdot (8.94 \cdot 10^{-8})^{\frac{4}{p_p+1}} (2.53 \cdot 10^{18})^{\frac{2(p_p-1)}{p_p+1}} f_{p_p}^{-\frac{4p_p-4}{p_p+1}} \xi_p^{\frac{4(p_p-2)}{(p_p+1)}} E_{54}^{-\frac{p_p+3}{p_p+1}} \epsilon_{p,-1}^{-\frac{4(p_p-1)}{(p_p+1)}} n_0^{-\frac{2}{p_p+1}},$$

which upon setting  $p_p = 2.3$  simplifies to

$$\epsilon_{B,-1} = 9.1 \times 10^5 \xi_p^{4/11} E_{54}^{-53/33} \epsilon_{p,-1}^{-52/33} n_0^{-20/33}. \quad (19)$$

This value of  $\epsilon_B$  may seem large, but so should be the kinetic energy of this burst, leading in fact to values of  $\epsilon_B$  smaller than unity, see the top panel plot on Figure 1.

Similarly, the acceleration efficiency parameter  $\alpha$  is obtained by comparing  $\nu_{\max,p}$  from Equation (13) with the observed energy of 7 TeV photon at  $t = 235$  s,

$$\alpha = 5.7 E_{54}^{1/8} n_0^{-1/8}. \quad (20)$$

To obtain the values of the other model parameters, we refer to *swift*-XRT data available at much later times, where XRT data is available and the emission is clearly in the "afterglow" phase in the *swift*-XRT band as well. We use Equation (16), which gives the expected energy flux above  $\nu_{m,e}$ , together with the observed *swift*-XRT flux at 3300 s of  $1.087 \times 10^{-7}$  erg s<sup>-1</sup> cm<sup>-2</sup> (at 0.3 keV) and include Equation (19) to get the injection fraction of electrons,

$$\xi_e \simeq (8.94 \cdot 10^{-8})^{\frac{1}{p_p+1}} (2.53 \cdot 10^{18})^{\frac{p_p-1}{2p_p+2}} 0.025^{-\frac{1}{p_e-2}} 6.44^{-\frac{p_e}{2(p_e-2)}} 10^{\frac{1-p_e}{p_e-2}} f_{p_e}^{\frac{p_e-1}{p_e-2}} f_{p_p}^{\frac{1-p_p}{p_p+1}} \\ \times E_{54}^{\frac{2p_p-p_e+4}{(2p_e-4)p_p+2p_e-4}} \epsilon_{e,-2}^{\frac{p_e-1}{p_e-2}} \epsilon_{p,-1}^{\frac{1-p_p}{p_p+1}} \xi_p^{\frac{p_p-2}{p_p+1}} n_0^{-\frac{1}{2p_p+2}}.$$

Setting  $p_e = 8/3$  and  $p_p = 23/10$  gives

$$\xi_e \simeq 0.11 E_{54}^{89/66} \xi_p^{1/11} \epsilon_{e,-2}^{5/2} n_0^{-5/33} \epsilon_{p,-1}^{-13/33}. \quad (21)$$

By balancing the *swift*-UVOT band flux of  $1.22 \times 10^{-8}$  erg s<sup>-1</sup> cm<sup>-2</sup> at observed energy 4.77 eV and observed time  $t = 4000$  s with the predicted synchrotron flux from Equation (15) and including Equations (19) and (21), we get

$$\epsilon_{e,-2} \approx 10 \cdot 0.025^{\frac{1}{p_e-1}} 0.06^{\frac{p_e-2}{p_e-1}} 6.44^{\frac{p_e}{2(p_e-1)}} E_{54}^{-1} f_{p_e}^{-1},$$

<sup>3</sup> [https://www.swift.ac.uk/xrt\\_live\\_cat/01126853/](https://www.swift.ac.uk/xrt_live_cat/01126853/)

<sup>4</sup> In the slow cooling regime, the requirement on the electrons power law index is even higher with  $p \sim 3$  for  $\nu_m < \nu_{XRT} < \nu_c$ .

<sup>5</sup> In the slow cooling regime, assuming  $\nu_m < \nu_{XRT} < \nu_c$ , the expected temporal decay in the TeV band is  $-2$ , for  $p = 3.0$ .

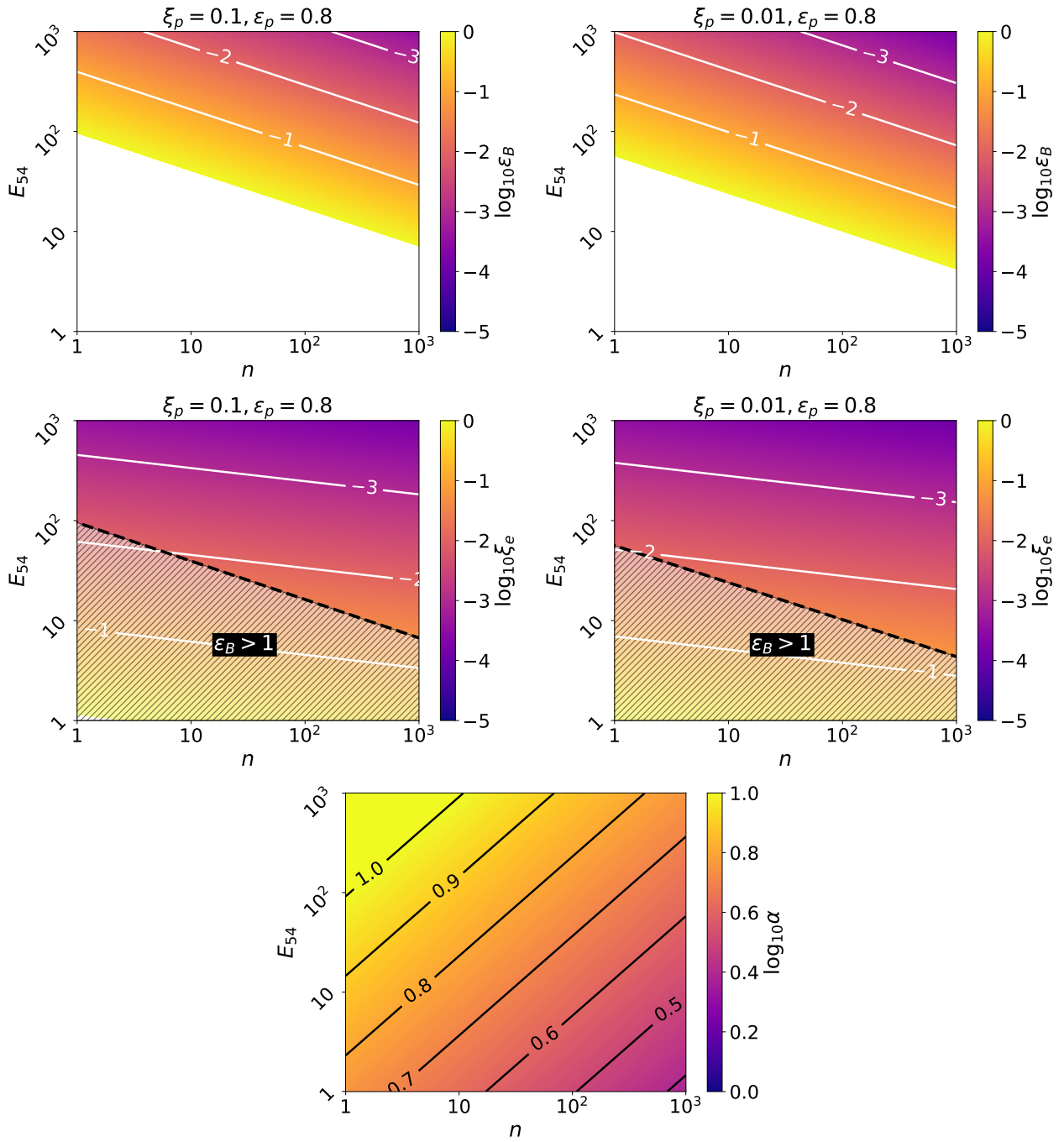


**Figure 1.** Parameters  $\epsilon_B$  (top) and  $\xi_e$  (middle) as functions of the total energy and ambient density,  $E_{54}$  and  $n_0$  for  $\epsilon_p = 0.8$  where assumed fraction of 10% of the protons are accelerated into a power law ( $\xi_p = 0.1$ , left) and 1% accelerated into a power law ( $\xi_p = 0.01$ , right). Bottom: the acceleration efficiency,  $\alpha$  as a function of  $E_{54}$  and  $n_0$ . The plots are obtained from Equations (19), (23), and (20), respectively. The white region is forbidden as it corresponds to  $\epsilon_B > 1$  as seen from the top panel. The assumptions  $p_e = 8/3$  and  $p_p = 2.3$  are enforced for these figures.

which gives for  $p_e = 8/3$

$$\epsilon_{e,-2} \approx 3.9 E_{54}^{-1}. \quad (22)$$

This enables to write the parameter  $\xi_e$  as

$$\xi_e = 0.06 \cdot (8.94 \cdot 10^{-8})^{\frac{1}{p_p+1}} (2.53 \cdot 10^{18})^{\frac{p_p-1}{2p_p+2}} f_{p_p}^{\frac{1-p_p}{p_p+1}} E_{54}^{\frac{-2p_p-3}{2p_p+2}} \epsilon_{p,-1}^{\frac{1-p_p}{p_p+1}} \xi_p^{\frac{p_p-2}{p_p+1}} n_0^{-\frac{1}{2p_p+2}},$$

which simplifies to

$$\xi_e = 3.2 \xi_p^{1/11} E_{54}^{-38/33} n_0^{-5/33} \epsilon_{p,-1}^{-13/33}, \quad (23)$$

for our chosen index values.

The values of  $\epsilon_B$ ,  $\alpha$  and  $\xi_e$ , as constrained by Equations (19), (20) and (23) are plotted in Figure 1 as functions of  $E_{54}$  and  $n_0$  for  $\epsilon_p = 0.8$  and two choices of  $\xi_p$ , namely  $\xi_p = 0.1$  (left column) and  $\xi_p = 0.01$  (right column). Satisfying  $\epsilon_B < 1$  directly requires that  $E_{54}$ ,  $n_0$  and  $\epsilon_p$  should be large while  $\xi_p$  needs to be small. Overall, we could constrain the parameters  $\epsilon_B$ ,  $\epsilon_e$ ,  $\xi_e$  and  $\alpha$  as functions of the other free model parameters. To provide satisfactory constraints with  $\epsilon_e + \epsilon_B + \epsilon_p < 1$ , the kinetic energy of this burst must be large with  $E_{54} > 10$ . Yet this is not too large compared to the prompt total isotropic energy. In fact, this high kinetic energy would correspond to an efficiency of around 10%, typical of other GRBs (see e.g. Zhang et al. 2007; Beniamini et al. 2016). We note that our goal here is to provide a set of parameters that could potentially explain the TeV observations via the proton synchrotron process and not to determine the best possible parameter values.

We thus find that a requirement of our model is that accelerated protons contribute for most of the internal energy of the shock, with  $\epsilon_p \gtrsim 0.1$ . The magnetic field needs to be strong,  $\epsilon_B \gtrsim 10^{-2}$ , and the circumburst density should be high,  $n_0 \gtrsim 10$ . All these require a high kinetic energy. Furthermore, the model requires that only a relatively small fraction of electrons and protons achieve a power-law distribution behind the shock, *i.e.*  $\xi_e \sim 10^{-2}$  and  $\xi_p \lesssim 10^{-1}$ , and that their spectral indices be different,  $p_e \neq p_p$ .

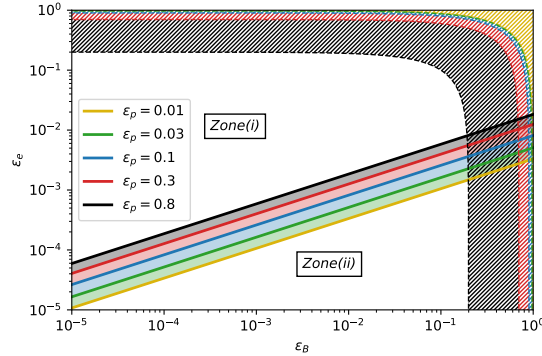


**Figure 2.** The parameter regime  $\epsilon_B$ ,  $\epsilon_e$  and  $\epsilon_p$  is explored in the context of  $p_e = 8/3$ ,  $p_p = 23/10$ ,  $E_{54} = 50$ ,  $n_0 = 50$ , corresponding to  $\xi_e = 0.01$  and  $\xi_p = 0.04$  for the condition (25). Notably, the proton-synchrotron process dominates mostly in regions where  $\epsilon_B > \epsilon_e$  (Zone (ii)), while the SSC process takes over when  $\epsilon_e > \epsilon_B$  (Zone (i)). Zone (ii) is shown to have different boundaries based on the value of  $\epsilon_p$  and these boundaries visually distinguish both the regions. It is clear that the dominance of proton synchrotron emission becomes more prominent as  $\epsilon_p$  increases. The hatched regions represent the condition  $\epsilon_B + \epsilon_p + \epsilon_e \leq 1$  for each  $\epsilon_p$  value and regarded as forbidden zones.

#### 4.2. Constraints imposed by the synchrotron-self Compton (SSC) emission.

In the SSC emission mechanism, the electrons that emit the low-energy synchrotron-photons inverse Compton (IC) scatter the same photons to higher energies, thus contributing to the high energy component of the afterglow spectrum. As we derive in details in appendix A, for the parameters chosen, this component is sub-dominant. Here we present the results only for  $p_e = 8/3$  and  $p_p = 23/10$ , but the general trend applies for other values of the injection index  $p_p$ . Within the framework of our model, the Klein-Nishina effect for the IC component can be neglected. This is shown by using Equations (1), (5) and (11) at  $t = 235$  s, to find

$$\frac{\gamma_{m,e} h \nu_{m,e}}{\Gamma} \sim 0.15 E_{54}^{5/33} \epsilon_{p,-1}^{13/33} n_0^{5/33} \xi_p^{-1/11} \text{ MeV}. \quad (24)$$



This result is in the order of (and even smaller than)  $m_e c^2$ , the energy at which the Klein-Nishina effect becomes important. One therefore only expects small modifications, if any, around the peak of the IC component.

The characteristic frequencies of the IC spectral component for this burst are presented in Appendix A. Equation (A2) gives the observed peak energy of the IC spectrum to be around  $h\nu_{m,IC} \sim 30$  GeV. To determine the criterion that governs the dominance of the proton-synchrotron component over the SSC component, we compare the fluxes at 1 TeV and at 235 s as  $[\nu F_\nu]_p/[\nu F_\nu]_{IC} \gtrsim 1$  (Zhang & Mészáros 2001). We can expand it using Equations (18), (17), (10) and (A5) to get the following:

$$0.15 E_{54}^{3/40} n_0^{7/12} \xi_e^{4/3} \xi_p^{-3/10} \epsilon_{B,-1}^{199/120} \epsilon_{p,-1}^{13/10} \epsilon_{e,-2}^{-10/3} \gtrsim 1. \quad (25)$$

This condition is displayed in Figure 2. The findings depicted in Figure 2 indicate the notion that  $\epsilon_B$  must exceed  $\epsilon_e$  in order to satisfy the above condition. Also it is evident that a near equipartition value of  $\epsilon_p$  reinforces the significant contribution from proton -synchrotron process.

From Equation (A5), the flux at 1 TeV and  $t_3 = 0.235$ , using the results of Equations (19) and (21) reads

$$[\nu F_\nu]_{IC|1 \text{ TeV}} = 3.4 \times 10^{-14} E_{54}^{313/396} \epsilon_{p,-1}^{182/99} n_0^{247/396} \xi_p^{-42/99} \text{ ergs cm}^{-2} \text{ s}^{-1}, \quad (26)$$

where we assumed that the TeV band is above the frequency of the IC spectral peak, and neglected Klein-Nishina effects. If anything, this effect would further reduce the observed flux in the TeV band, and allow for a larger parameter space in which the proton synchrotron mechanism dominates. This value is  $\approx 8$  orders of magnitude lower than the observed flux at the TeV band, implying that the electron SSC mechanism is sub-dominant at these energies for the constraints we derived.

## 5. LIGHTCURVE AND SPECTRA

The observed lightcurve of the afterglow of GRB 221009A is shown in Figure 3 alongside the electron and proton synchrotron components estimated from our model. The two different set of parameters used in this section are summarized in Table 1. We set the parameters to  $p_e = 8/3$ ,  $p_p = 2.3$ ,  $E_{54} = 50$ ,  $n_0 = 50$ ,  $\epsilon_{p,-1} = 8$  and  $\xi_p = 0.04$ , resulting in  $\epsilon_{B,0} = 0.186$ ,  $\epsilon_{e,0} = 0.0014$  and  $\xi_e = 0.01$ . The onset of the afterglow phase at 226 s after the burst trigger is marked by the dotted line (LHAASO-Collaboration et al. 2023) whereas the dashed line drawn at  $t = 597$  s marks the end of the prompt duration estimated by Lesage et al. (2023). Overall, this figure demonstrates that the proton synchrotron model presented here is capable of explaining the observed temporal features of the afterglow of GRB 221009A in several different energy bands.

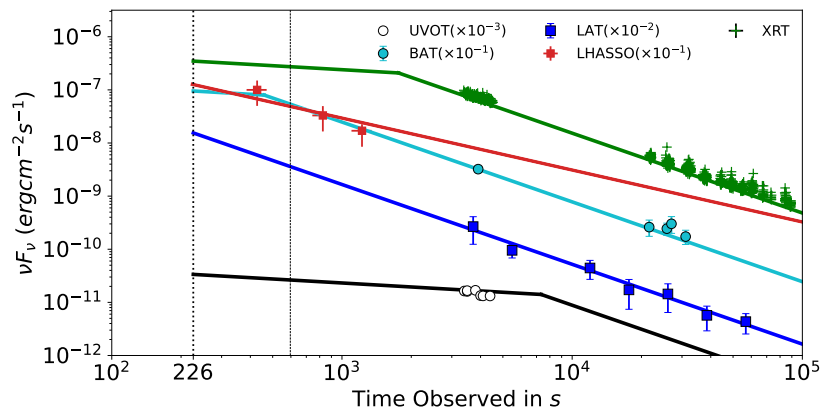


**Figure 3.** The multi-wavelength afterglow light curve for the proton synchrotron model along with the observed data of GRB 221009A for  $p_e = 8/3$ ,  $p_p = 23/10$ ,  $E_{54} = 50$ ,  $n_0 = 50$ ,  $\epsilon_{p,-1} = 8$  and  $\xi_p = 0.04$ , corresponding to  $\epsilon_{B,0} = 0.186$ ,  $\epsilon_{e,0} = 0.0014$  and  $\xi_e = 0.01$ . The *swift*-UVOT (white filter) and BAT data were retrieved from Tables 4 and 6 of Williams et al. (2023) and the *fermi*-LAT data were obtained from Table 5 of Laskar et al. (2023b). The optical data is corrected for galactic extinction with  $A_v = 5.4$  (Shrestha et al. 2023; Fulton et al. 2023). The black dotted line at 226 s marks the onset of the afterglow phase corresponding to LHAASO-Collaboration et al. (2023), while the black dashed line at  $T_0 = 597$  s marks the afterglow onset determined by Lesage et al. (2023).

We further produce the afterglow spectrum at two different times, namely at  $t = 235$  s and  $t = 4000$  s, and display it in Figure 4 (both in the left and right panels). The spectral energy distributions (hereinafter SEDs) consist of three main components. They are produced by the electron-synchrotron, the proton-synchrotron and the IC processes and are respectively shown by the blue, red and black lines. Inspection of Figure 4 (left), obtained for  $p_e = 8/3$  and  $p_p = 2.3$ , shows that the SED of the electron-synchrotron component at 4000 s satisfies the observed data in the optical and X-ray bands as designed in our analytic approach. At the same time, the proton synchrotron component accounts for the LHAASO flux, also marginally satisfies the LAT flux.

We then search for solutions with a smaller proton index,  $p_p = 2.2$ . This is advantageous as it results in a lower burst energy and external density. The right panel of Figure 4 shows the SEDs for the parameters  $E_{54} = 30$ ,  $n_0 = 30$ ,  $\xi_p = 0.1$ ,  $\epsilon_{p,-1} = 8$ , resulting in  $\epsilon_B = 0.17$ ,  $\xi_e = 0.01$ ,  $\epsilon_e = 0.002$  and  $\alpha = 6$ . In addition, under this assumption, the required total burst energy  $E$  is lower than for  $p_p = 2.3$ . Hence the prompt radiative efficiency is increased here. We see that, in this case too, the LAT flux at 4000 s can be marginally explained by the proton synchrotron process.

The close to equipartition values of  $\epsilon_B$  and  $\epsilon_p$  associated with all the SEDs are as anticipated for the proton-synchrotron model, see Equations (19) and (23). Indeed, protons are more massive than electrons and to radiate a substantial amount of energy, they need a strong magnetic field. We further find that the IC components (black lines in the SEDs shown in Figure 4) are subdominant at all time bins in both scenarios considered, since the magnetic field energy density is large compared to the electron energy density ( $U_B \gg U_e$ , see e.g. Rybicki & Lightman 1986). Indeed, for the constraints we derived, using  $p_e = 8/3$  and  $p_p = 23/10$ , one obtains

$$U_B = 2.1 \times 10^6 E_{54}^{-179/132} \epsilon_{p,-1}^{-52/33} n_0^{19/132} t_3^{-3/4} \xi_p^{4/11},$$

$$\text{and } U_e = 0.14 E_{54}^{-7/8} n_0^{7/8} t_3^{-7/8}.$$

The corresponding ratios of the energy densities in our models are given in Table 1.

The lightcurve of the TeV emission is shown to have a break followed by a steeper temporal decay at time  $T_0 + 896 (+230, -110)$  s (LHAASO-Collaboration et al. 2023). This break could be obtained by the crossing of the maximum synchrotron frequency  $\nu_{\max}$  through the LHAASO energy band. For the parameters we derived in case  $p_e = 8/3$  and  $p_p = 2.3$ , the time at which  $\nu_{\max}$  equals 1 TeV is  $t_3 = 42$ . In principle, it is possible to use this property to better constrain the acceleration efficiency,  $\alpha$  and the other model parameters. However, this constraint depends on the exact parametrization of the proton distribution function at the highest energies, and therefore would bring only little insight into the model, apart from better constraining  $\alpha$ .

## 6. DISCUSSION

### 6.1. Comparison between GRB 221009A and GRB 190114C

Similar to GRB 221009A, GRB 190114C is another long GRB with a VHE afterglow emission observed in the band between 0.2 and 1 TeV (Acciari et al. 2019b). This GRB has an isotropic equivalent energy  $E_{iso} \simeq 2.5 \times 10^{53}$  erg. The redshifts of both GRB 190114C ( $z = 0.4245$ ) and GRB 221009A are low,  $z < 0.5$ . As a result, the detectability of  $\geq 1$  TeV photons, if produced in the source, is high, since they are only weakly EBL attenuated (see e.g. Franceschini 2021). Similarly to GRB 221009A, a complete set of multi-wavelength observational data is available for GRB 190114C afterglow (see e.g. MAGIC Collaboration et al. 2019, for a summary of those observations). In Isravel et al. (2022), we considered the proton synchrotron mechanism to explain the VHE afterglow of GRB 190114C.

One can therefore compare the parameters we derived for GRB 221009A to those we obtained for GRB 190114C, in order to outline some of the intriguing features of long GRB associated to VHE energy afterglow observations. Under the guise of a proton synchrotron model, these features are as follows:

#### 6.1.1. Particle index

The parameters associated with  $p_e \neq p_p$  yielded the most optimal results in these bursts. One potential cause of protons and electrons having distinct indices is the non-uniformity of the power-law turbulence spectrum of the

**Table 1.** Parameters used to construct the SEDs in Figure 4.

	$p_e$	$p_p$	$E$	$n$	$\xi_p$	$\epsilon_p$	$\epsilon_B$	$\epsilon_e$	$\xi_e$	$\alpha$	$\eta$	$U_B/U_e$
Figure 4 left	8/3	2.3	$5 \times 10^{55}$ erg	$50 \text{ cm}^{-3}$	0.04	0.8	$18.57 \times 10^{-2}$	$1.4 \times 10^{-3}$	0.01	6	5.7%	$8.1 \times 10^3 t_3^{-3/8}$
Figure 4 right	8/3	2.2	$3 \times 10^{55}$ erg	$30 \text{ cm}^{-3}$	0.1	0.8	$17 \times 10^{-2}$	$2 \times 10^{-3}$	0.01	6	9.1%	$5.2 \times 10^3 t_3^{-3/8}$

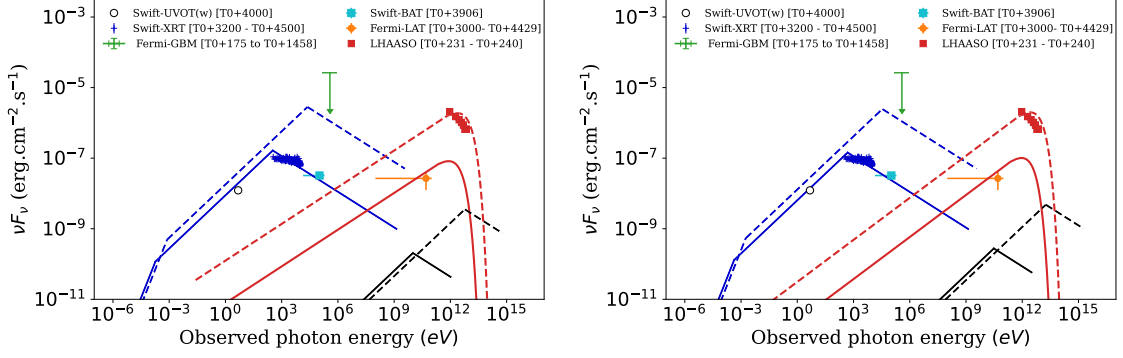


**Figure 4.** Left: the spectral energy distributions for  $p_e = 8/3$  and  $p_p = 23/10$  at different times,  $t = 235$  s (dashed) and  $t = 4000$  s (solid). The parameters are  $E_{54} = 50$ ,  $n_0 = 50$ ,  $\epsilon_{p,-1} = 8$  and  $\xi_p = 0.04$ , leading to  $\epsilon_B = 0.186$ ,  $\epsilon_e = 0.0014$ ,  $\xi_e = 0.01$  and  $\alpha = 6$ . Right: the spectral energy distributions for for  $p_e = 8/3$  and  $p_p = 22/10$ , the other parameters are  $E_{54} = 30$ ,  $n_0 = 30$ ,  $\epsilon_{p,-1} = 8$  and  $\xi_p = 0.1$ , corresponding to  $\epsilon_B = 0.17$ ,  $\epsilon_e = 0.002$ ,  $\xi_e = 0.01$  and  $\alpha = 6$ . The blue line represents the electron synchrotron component, the red line represents the proton synchrotron emission and the black line specifies the IC component.

magnetic field across a wide range of scales (Asano et al. 2009). This could be realized under several circumstances: a) a difference in scales corresponding to the gyration radii of protons attaining  $10^{20}$  eV, and electrons reaching GeV energies (Cerruti et al. 2015), respectively, and b) a variation in wavelength distribution of shock generated magnetic perturbations and geometry of the magnetic field at the shock front (Niemić et al. 2006). On the other hand, the acceleration processes setting these power-law indices in the presence of shock can have varied properties depending upon the orientation of the magnetic field relative to the shock (Caprioli & Spitkovsky 2014a,b; Guo et al. 2014). Apart from these, a two-component jet model could also feature different power law indices. In this model, a narrow, highly collimated jet could account for the TeV emission produced by protons, while a less collimated, wider jet could be responsible for the low-energy emission from electrons (Berger et al. 2003; Huang et al. 2004; Sato et al. 2023).

### 6.1.2. Embedded magnetic field

Requiring that proton synchrotron emission explains the TeV observations results in the necessity of having a strong magnetic field, with  $\epsilon_B$  close to equipartition. Similarly, the electron equipartition energy must be low,  $\epsilon_e \lesssim 10^{-3}$ . Even though the inference  $\epsilon_B \sim 10^{-1}$  is inconsistent with the analytical models and particle-in-cell (PIC) simulations of un-magnetized plasma (Medvedev 2006; Sironi & Spitkovsky 2011), such a relatively high  $\epsilon_B$  can be possibly explained as follows. Considering the connection between long-GRBs and supernovae could account for the highly magnetized environment as well as low  $\epsilon_e$  (see e.g. Kippen et al. 1998; Bosnjak et al. 2006; Campana et al. 2006; Klose et al. 2019). By performing global fitting of the emission in six supernova remnants (SNRs), Reynolds et al. (2021) found  $\epsilon_B$  to be between  $10^{-3}$  and  $10^{-1}$ , while  $\epsilon_e$  achieves a smaller value in the range of  $10^{-4} - 5 \cdot 10^{-2}$ . These equipartition parameters were determined owing to the advantageous conditions provided by SNRs. This is analogous to the findings in our model for this GRB and 190114C (Isravel et al. 2022). Also, the compression of the upstream turbulent magnetic field by the shock may amplifies its strength (Lemoine & Revenu 2006). The type of turbulence spectrum may also dictate the strength of the magnetic field, such as Kolmogorov turbulence (Biermann & Strittmatter 1987) and Kraichnan turbulence (Kraichnan 1965). Alternatively, the reverse shock approximation could also be evoked for proton acceleration as it could harbor such a high magnetization (Waxman & Bahcall 2000; Zhang et al. 2018). To explain the VHE emission of GRB 221009A with synchrotron emission from protons accelerated at the reverse shock, Zhang et al. (2022) implemented a strong magnetic field with  $\epsilon_B \sim 0.5$ .

### 6.1.3. Injection fraction

The measured fluxes, together with the large kinetic energy, require the fraction of particle accelerated into the power-law to be considerably low,  $\xi_e \approx 10^{-2}$  and  $\xi_p \approx 10^{-2}$ . These values are consistent with the numerical estimation of  $\xi_e \lesssim 10^{-1}$  considering the acceleration of charged particles in collisionless shocks (Sironi & Spitkovsky 2011). A lower than the unity  $\xi$  is gaining attention in the GRB afterglow theories and modeling, see e.g. Ressler & Laskar (2017); Warren et al. (2018); Cunningham et al. (2020); Asano et al. (2020). For instance, for the very nearby ( $z \sim 0.07$ ), GRB

190829A,  $\xi < 1$  is obtained by a fit to the data (Salafia et al. 2022). Also, Gill & Granot (2023) concluded their investigation of GRB 221009A by emphasizing the small value of  $\xi_e \sim 10^{-2}$  required by their analysis. Such a low injection fraction of electrons and protons indicate that there is a large population of thermal particle species present in the downstream of the shock (Ressler & Laskar 2017). The thermal particles can indeed be anticipated to emit synchrotron radiation in radio frequencies during the early phase according to Eichler & Waxman (2005). However, the contribution of these thermal electrons and protons in producing the GRB spectra is yet to be studied in detail (Warren et al. 2018).

#### 6.1.4. Progenitor environment

The progenitor of long-GRBs is a massive star which collapses to form a compact object (see *e.g.* Kumar & Zhang 2015). The low-metallicity Wolf-Rayet stars ( $20 - 25M_{\odot}$ ) with low mass-loss rates ( $\sim 10^{-7}M_{\odot}\text{yr}^{-1}$ ) are believed to be progenitors for the collapsar model for which the circumburst density is  $n \gtrsim 10 \text{ cm}^{-3}$  (Woosley et al. 2002; Fryer et al. 2006). Considering  $\xi = 0.01$  in our model, the external medium density of these long duration bursts ranges between  $10 - 10^2 \text{ cm}^{-3}$ . When  $\xi = 1$ , for a constant ISM medium, the circumburst density estimated in theoretical models is around  $n \leq 1 \text{ cm}^{-3}$  (Beniamini et al. 2015; Gompertz et al. 2018; Derishev & Piran 2021b; Guarini et al. 2023), and can even reach  $\sim 100 \text{ cm}^{-3}$  (Laskar et al. 2015) in some specific cases.

#### 6.1.5. Energetics of GRBs

For those two bursts, the required kinetic energy is larger by about an order of magnitude than their prompt-phase equivalent energy  $E_{iso}$ . This leads to a radiative efficiency  $\eta = E_{iso}/(E_k + E_{iso})$  in the order of 10%. For the proton synchrotron model, we estimated  $\eta$  to be about 8% for GRB 190114C and 9% for GRB 221009A considering  $p_e = 8/3$  and  $p_p = 2.2$  for the latter. Moreover, if the jet observed in GRB 221009A is considerably narrow with a half-opening angle of  $\theta \sim 0.8^\circ$  as reported by LHAASO-Collaboration et al. (2023), then the jet kinetic energy after correcting for beaming is  $E_{k,jet} = (\theta^2/2)E_k \sim 3 \times 10^{51} \text{ erg}$  for  $p_e = 8/3$  and  $p_p = 2.2$  while for  $p_e = 8/3$  and  $p_p = 2.3$  it is  $E_{k,jet} \sim 5 \times 10^{51} \text{ erg}$ . This is in agreement with the expectations of amount of energy stored in GRBs (Frail et al. 2001). This analysis is based on the Konus-Wind estimation of  $E_{iso} \sim 3 \times 10^{54} \text{ erg}$  (Frederiks et al. 2022). However, *Insight-HXMT* in conjunction with the GECAM-C measured the isotropic equivalent energy of GRB 221009A to be  $1.5 \times 10^{55} \text{ erg}$  (An et al. 2023). The latter measurement is five times higher than the former. It is worthy to highlight that integrating  $E_{iso} = 1.5 \times 10^{55} \text{ erg}$  into our model leads to an increase in  $\eta$  which is around 33% for  $p_e = 8/3$  and  $p_p = 2.2$  and  $\sim 23\%$  considering  $p_e = 8/3$  and  $p_p = 2.3$ , while the other parameters remain unchanged. We emphasize that both estimates of  $E_{iso}$  values yield reasonable prompt phase-energy conversion efficiencies.

#### 6.1.6. Acceleration Efficiency

Finally, we found that these bursts do not require a very efficient proton acceleration, with an efficiency in the order of a few tens,  $\alpha \approx 5 - 20$ . Interestingly, the PIC simulations performed in Asano et al. (2020) in the context of the VHE afterglow emission of GRB 190114C resulted in even lower efficiency,  $\alpha \sim 100$ . It is obtained by considering the early diffusive process in Fermi acceleration mechanism. The parameter  $\alpha$  in the range  $5 - 20$  acquired by setting the maximum proton energy may imply that high energy protons could be accelerated via MHD turbulence (Demidem et al. 2018; Asano et al. 2020).

### 6.2. Comparison of SSC and proton-synchrotron components for GRB 221009A

Many authors attempt to explain the VHE observations of GRB afterglow with a purely leptonic modeling based on the synchrotron self-Compton process (for instance Zhang et al. 2022; González et al. 2022; Ren et al. 2022; Laskar et al. 2023a; Kann et al. 2023; Das & Razaque 2023; LHAASO-Collaboration et al. 2023). It is argued that explaining the high energy photon with this mechanism is difficult because the modelled SSC flux in the TeV band, which is strongly constrained by the radio, optical and X-ray fluxes, is smaller than the corresponding observed flux after correcting for the EBL absorption (see, González et al. 2022; Miceli & Nava 2022). The obtained fits required lower magnetization than the one presented here, typically  $\epsilon_B \approx 10^{-4} - 10^{-3}$  and higher  $\epsilon_e \approx 10^{-2} - 10^{-1}$ .

In the model we presented, this problem does not exist. Indeed the flux in the TeV band is somewhat independent from the flux at lower energies. However, this freedom comes at the expense of a large kinetic energy and a small fraction of electrons injected into the non-thermal power-law. This ultimately leads to a large external density for the interstellar medium and a small (5 to 10 %) prompt radiative efficiency. We stress that these values are consistent with those found in numerical simulations, as well as afterglow modelling.

## 7. CONCLUSIONS

The explosions caused by the core collapse of massive stars are predicted to result in long-GRBs (see *e.g.* Kumar & Zhang 2015). Some of them, as identified recently, are accompanied by VHE signals at energies  $\gtrsim$  TeV during their afterglow phase. This offers an opportunity to investigate the source of VHE emission from these extremely powerful events. We have explained the early afterglow of GRB 221009A within the framework of a hybrid emission model where the electron-synchrotron process is the source of the low energy component of the spectrum and the VHE component is explained by the proton-synchrotron mechanism with different particle indices. We constrain some parameters of this model by using observations in the optical, X-ray and TeV bands, and demonstrate that the observations can be reproduced by our model. Yet, our modeling requires that protons and electrons have different spectral indices. The key aspect of our model is that the kinetic energy of the bursts needs to be large and the fraction of particles (electrons and protons) accelerated into the power-law must be small.

We then compare the model parameters we obtained for GRB 221009A and for GRB 190114C (Isravel et al. 2022) to underline their similarity. We find that explaining these two bursts with the hybrid model we presented requires a large kinetic energy,  $E$  and density,  $n$ , which in turn limits the fractions of accelerated particles injected into the power-law by shock acceleration to be small, with  $\xi_e \sim 10^{-2}$  and  $\xi_p \gtrsim 10^{-2}$ . Still, we emphasize the fact that the required energy in both cases,  $\approx 10^{54} - 10^{55}$  erg is not unacceptable. Especially for these extremely bright GRBs, the efficiency in kinetic energy conversion to prompt emission is of the order of a few percent and up to 10%. These values are not exceptional. Similar constraints are commonly inferred in GRBs, under various assumptions: for example in the context of purely leptonic models, see Cunningham et al. (2020). The existence of a strong magnetic field, characterized by  $\epsilon_B \gg \epsilon_e$  is crucial for a proton-synchrotron process to explain the TeV emission. We demonstrated that under this assumption, the high energy component of the SSC model experiences a significant suppression. However, the SSC process may take precedence in a scenario where  $\epsilon_B \ll \epsilon_e$ .

We therefore conclude that the proton-synchrotron process offers a compelling alternative to other radiative models based on the SSC mechanisms to explain the VHE afterglow of the GRBs. Further detection of GRBs at VHE by the Cherenkov telescope array (CTA) (Knödlseder 2020) and the LHAASO experiment will allow to further constrain the free parameters and contrast it with other purely leptonic models.

We acknowledge support from the European Research Council via ERC consolidating grant No. 773062 (acronym O.M.J.).

## APPENDIX

### A. INVERSE-COMPTON (IC) SCATTERING COMPONENT

First we point out that in our model we can adapt the classical regime for the inverse Compton process, *i.e.* neglect Klein-Nishina effects. Indeed

$$\gamma_{m,e} h\nu_{m,e} \Gamma^{-1} \sim 0.15 E_{54}^{5/33} \epsilon_{p,-1}^{13/33} n_0^{5/33} \xi_p^{-1/11} \text{ MeV}. \quad (\text{A1})$$

Hence, the minimum frequency of the up-scattered electrons in the observer's frame of reference is given by  $\nu_{m,IC} = 2\gamma_{m,e}^2 \nu_{m,e}$ . Using Equations (19) and (21) at  $t = 235$  s and  $p_e = 2.67$ , we find

$$\begin{aligned} h\nu_{m,IC} &= 1.58 \times 10^{17} 0.025^{\frac{4}{p_e-1}} 0.06^{\frac{4(p_e-2)}{p_e-1}} 6.44^{\frac{2p_e}{p_e-1}} (2.53 \cdot 10^{18})^{\frac{1-p_p}{p_p+1}} (8.94 \cdot 10^{-8})^{-\frac{2}{p_p+1}} f_p^{\frac{2p_p-2}{p_p+1}} \\ &\quad \times E_{54}^{\frac{p_p+5}{4p_p+4}} \epsilon_{p,-1}^{\frac{2p_p-2}{p_p+1}} n_0^{\frac{3-p_p}{4p_p+4}} \xi_p^{\frac{4-2p_p}{p_p+1}}, \\ &= 30 E_{54}^{73/132} \epsilon_{p,-1}^{26/33} n_0^{7/132} \xi_p^{-2/11} \text{ GeV}, \end{aligned} \quad (\text{A2})$$



Similarly, the characteristic cooling energy of the IC spectrum,  $\nu_{c,IC} = 2\gamma_{c,e}^2 \nu_{c,e}$ , is given by

$$\begin{aligned} h\nu_{c,IC} &= 1.55 \times 10^8 (8.94 \cdot 10^{-8})^{-\frac{14}{p_p+1}} (2.53 \cdot 10^{18})^{-\frac{7(p_p-1)}{p_p+1}} f_{p_p}^{\frac{14p_p-14}{p_p+1}} E_{54}^{\frac{9p_p+37}{4p_p+4}} \epsilon_{p,-1}^{\frac{14p_p-14}{p_p+1}} \\ &\quad \times n_0^{\frac{19-9p_p}{4p_p+4}} \xi_p^{\frac{28-14p_p}{p_p+1}}, \\ &= 6.8 \times 10^{-17} E_{54}^{577/132} \epsilon_{p,-1}^{182/33} n_0^{-17/132} \xi_p^{-14/11} \text{ eV}. \end{aligned} \quad (\text{A3})$$

The maximum flux of the IC spectrum is given by  $F_{\nu_{\text{peak},IC}} = \frac{1}{3} \sigma_T n_e r F_{\nu_{\text{peak},e}}$ , and is expressed as

$$\begin{aligned} F_{\nu_{\text{peak},IC}} &= 3.51 \times 10^{-32} (2.53 \cdot 10^{18})^{\frac{2p_p-2}{p_p+1}} (8.94 \cdot 10^{-8})^{\frac{4}{p_p+1}} f_{p_p}^{\frac{4-4p_p}{p_p+1}} E_{54}^{\frac{-5p_p-13}{4p_p+4}} \epsilon_{p,-1}^{\frac{4-4p_p}{p_p+1}} n_0^{\frac{5p_p-3}{4p_p+4}} \xi_p^{\frac{4p_p-8}{p_p+1}}, \\ &= 3.2 \times 10^{-25} E_{54}^{-245/132} \epsilon_{p,-1}^{-52/33} \xi_p^{4/11} n_0^{85/132} \text{ erg cm}^{-2} \text{ s}^{-1} \text{ Hz}^{-1}. \end{aligned} \quad (\text{A4})$$

Considering Equations (A2) and (A3), clearly  $\nu_{m,IC} > \nu_{c,IC}$ . The IC flux at 1 TeV for  $p_e = 8/3$  and  $t = 235$  s is then estimated to be

$$\begin{aligned} [\nu F_\nu]_{IC}|_{1 \text{ TeV}} &= 2.28 \times 10^{-5} 0.543^{\frac{p_e}{2}} 10^{\frac{2-7p_e}{4}} f_{p_e}^{2p_e-2} E_{54}^{\frac{3p_e+2}{8}} \epsilon_{B,-1}^{\frac{p_e-6}{4}} \epsilon_{e,-2}^{2p_e-2} n_0^{\frac{2-p_e}{8}} \xi_e^{4-2p_e}, \\ &= 1.7 \times 10^{-10} E_{54}^{5/4} \epsilon_{e,-2}^{10/3} \epsilon_{B,-1}^{-5/6} n_0^{-1/12} \xi_e^{-4/3} \text{ erg cm}^{-2} \text{ s}^{-1}. \end{aligned} \quad (\text{A5})$$

## REFERENCES

- Abdalla, H., Adam, R., Aharonian, F., et al. 2019, *Nature*, 575, 464, doi: [10.1038/s41586-019-1743-9](https://doi.org/10.1038/s41586-019-1743-9)
- Acciari, V. A., Ansoldi, S., Antonelli, L. A., et al. 2019a, *Nature*, 575, 459, doi: [10.1038/s41586-019-1754-6](https://doi.org/10.1038/s41586-019-1754-6)
- Acciari, V. A., et al. 2019b, *Nature*, 575, 459, doi: [10.1038/s41586-019-1754-6](https://doi.org/10.1038/s41586-019-1754-6)
- Ackermann, M., Ajello, M., Allafort, A., et al. 2012, *Science*, 338, 1190, doi: [10.1126/science.1227160](https://doi.org/10.1126/science.1227160)
- Aharonian, F. A., Hofmann, W., Konopelko, A. K., & Völk, H. J. 1997, *Astroparticle Physics*, 6, 369, doi: [10.1016/S0927-6505\(96\)00070-9](https://doi.org/10.1016/S0927-6505(96)00070-9)
- An, Z.-H., Antier, S., Bi, X.-Z., et al. 2023, arXiv e-prints, arXiv:2303.01203, doi: [10.48550/arXiv.2303.01203](https://doi.org/10.48550/arXiv.2303.01203)
- Asano, K., Inoue, S., & Mészáros, P. 2009, *ApJ*, 699, 953, doi: [10.1088/0004-637X/699/2/953](https://doi.org/10.1088/0004-637X/699/2/953)
- Asano, K., Murase, K., & Toma, K. 2020, *ApJ*, 905, 105, doi: [10.3847/1538-4357/abc82c](https://doi.org/10.3847/1538-4357/abc82c)
- Beniamini, P., Nava, L., Duran, R. B., & Piran, T. 2015, *MNRAS*, 454, 1073, doi: [10.1093/mnras/stv2033](https://doi.org/10.1093/mnras/stv2033)
- Beniamini, P., Nava, L., & Piran, T. 2016, *MNRAS*, 461, 51, doi: [10.1093/mnras/stw1331](https://doi.org/10.1093/mnras/stw1331)
- Berger, E., Kulkarni, S. R., Pooley, G., et al. 2003, *Nature*, 426, 154, doi: [10.1038/nature01998](https://doi.org/10.1038/nature01998)
- Biermann, P. L., & Strittmatter, P. A. 1987, *ApJ*, 322, 643, doi: [10.1086/165759](https://doi.org/10.1086/165759)
- Blanch, O., Longo, F., Berti, A., et al. 2020, *GRB Coordinates Network*, 29075, 1
- Blandford, R. D., & McKee, C. F. 1976, *Physics of Fluids*, 19, 1130, doi: [10.1063/1.861619](https://doi.org/10.1063/1.861619)
- Bosnjak, Z., Celotti, A., Ghirlanda, G., Della Valle, M., & Pian, E. 2006, *A&A*, 447, 121, doi: [10.1051/0004-6361:20052803](https://doi.org/10.1051/0004-6361:20052803)
- Böttcher, M., & Dermer, C. D. 1998, *ApJL*, 499, L131, doi: [10.1086/311366](https://doi.org/10.1086/311366)
- Cai, C., et al. 2021, *Mon. Not. Roy. Astron. Soc.*, 508, 3910, doi: [10.1093/mnras/stab2760](https://doi.org/10.1093/mnras/stab2760)
- Campana, S., Mangano, V., Blustin, A. J., et al. 2006, *Nature*, 442, 1008, doi: [10.1038/nature04892](https://doi.org/10.1038/nature04892)
- Cao, Z., della Volpe, D., Liu, S., et al. 2019, arXiv e-prints, arXiv:1905.02773. <https://arxiv.org/abs/1905.02773>
- Caprioli, D., & Spitkovsky, A. 2014a, *ApJ*, 783, 91, doi: [10.1088/0004-637X/783/2/91](https://doi.org/10.1088/0004-637X/783/2/91)
- . 2014b, *ApJ*, 794, 47, doi: [10.1088/0004-637X/794/1/47](https://doi.org/10.1088/0004-637X/794/1/47)
- Castro-Tirado, A. J., Sanchez-Ramirez, R., Hu, Y. D., et al. 2022, *GRB Coordinates Network*, 32686, 1
- Cerruti, M., Zech, A., Boisson, C., & Inoue, S. 2015, *MNRAS*, 448, 910, doi: [10.1093/mnras/stu2691](https://doi.org/10.1093/mnras/stu2691)
- Cunningham, V., Cenko, S. B., Ryan, G., et al. 2020, *ApJ*, 904, 166, doi: [10.3847/1538-4357/abc2cd](https://doi.org/10.3847/1538-4357/abc2cd)
- Das, S., & Razzaque, S. 2023, *A&A*, 670, L12, doi: [10.1051/0004-6361/202245377](https://doi.org/10.1051/0004-6361/202245377)
- de Ugarte Postigo A., Izzo, L., & Pugliese, G. e. a. 2022, *GRB 221009A: Redshift from X-shooter/VLT*. <https://gcn.gsfc.nasa.gov/gcn3/32648.gcn3>
- Demidem, C., Lemoine, M., & Casse, F. 2018, *MNRAS*, 475, 2713, doi: [10.1093/mnras/stx3367](https://doi.org/10.1093/mnras/stx3367)
- Derishev, E., & Piran, T. 2021a, arXiv e-prints, arXiv:2106.12035. <https://arxiv.org/abs/2106.12035>



- . 2021b, *ApJ*, 923, 135, doi: [10.3847/1538-4357/ac2dec](https://doi.org/10.3847/1538-4357/ac2dec)
- Dermer, C. D., Chiang, J., & Mitman, K. E. 2000, *The Astrophysical Journal*, 537, 785, doi: [10.1086/309061](https://doi.org/10.1086/309061)
- Dichiara, S., Gropp, J. D., Kennea, J. A., et al. 2022, *The Astronomer's Telegram*, 15650, 1
- Eichler, D., & Waxman, E. 2005, *ApJ*, 627, 861, doi: [10.1086/430596](https://doi.org/10.1086/430596)
- Evans, P. A., Beardmore, A. P., Page, K. L., et al. 2007, *A&A*, 469, 379, doi: [10.1051/0004-6361:20077530](https://doi.org/10.1051/0004-6361:20077530)
- . 2009, *MNRAS*, 397, 1177, doi: [10.1111/j.1365-2966.2009.14913.x](https://doi.org/10.1111/j.1365-2966.2009.14913.x)
- Fraija, N., Dainotti, M. G., Ugale, S., Jyoti, D., & Warren, D. C. 2022, *ApJ*, 934, 188, doi: [10.3847/1538-4357/ac7a9c](https://doi.org/10.3847/1538-4357/ac7a9c)
- Fraija, N., Duran, R. B., Dichiara, S., & Beniamini, P. 2019, *The Astrophysical Journal*, 883, 162
- Frail, D. A., Kulkarni, S. R., Sari, R., et al. 2001, *ApJL*, 562, L55, doi: [10.1086/338119](https://doi.org/10.1086/338119)
- Franceschini, A. 2021, *Universe*, 7, 146, doi: [10.3390/universe7050146](https://doi.org/10.3390/universe7050146)
- Frederiks, D., A.Lysenko, Ridnaia, A., et al. 2022, *Konus-Wind detection of GRB 221009A*. <https://gcn.gsfc.nasa.gov/gcn3/32668.gcn3>
- Frederiks, D., Svinkin, D., Lysenko, A. L., et al. 2023, *arXiv e-prints*, arXiv:2302.13383, doi: [10.48550/arXiv.2302.13383](https://doi.org/10.48550/arXiv.2302.13383)
- Fryer, C. L., Rockefeller, G., & Young, P. A. 2006, *ApJ*, 647, 1269, doi: [10.1086/505590](https://doi.org/10.1086/505590)
- Fulton, M. D., Smartt, S. J., Rhodes, L., et al. 2023, *ApJL*, 946, L22, doi: [10.3847/2041-8213/acc101](https://doi.org/10.3847/2041-8213/acc101)
- Ghisellini, G., & Celotti, A. 1998, *The Astrophysical Journal*, 511, L93
- Gill, R., & Granot, J. 2023, *arXiv e-prints*, arXiv:2304.14331, doi: [10.48550/arXiv.2304.14331](https://doi.org/10.48550/arXiv.2304.14331)
- Gompertz, B. P., Fruchter, A. S., & Pe'er, A. 2018, *ApJ*, 866, 162, doi: [10.3847/1538-4357/aadba8](https://doi.org/10.3847/1538-4357/aadba8)
- González, M. M., Avila Rojas, D., Pratts, A., et al. 2022, *arXiv e-prints*, arXiv:2210.15857, doi: [10.48550/arXiv.2210.15857](https://doi.org/10.48550/arXiv.2210.15857)
- Guarini, E., Tamborra, I., Bégué, D., & Rudolph, A. 2023, *MNRAS*, 523, 149, doi: [10.1093/mnras/stad1421](https://doi.org/10.1093/mnras/stad1421)
- Guo, X., Sironi, L., & Narayan, R. 2014, *ApJ*, 794, 153, doi: [10.1088/0004-637X/794/2/153](https://doi.org/10.1088/0004-637X/794/2/153)
- H. E. S. S. Collaboration, Abdalla, H., Aharonian, F., et al. 2021, *Science*, 372, 1081, doi: [10.1126/science.abe8560](https://doi.org/10.1126/science.abe8560)
- Hu, Y.-D., Casanova, V., & Fernandez-Garcia, E., e. a. 2022, *GRB 221009A BOOTES-2/TELMA and OSN optical detections*. <https://gcn.gsfc.nasa.gov/gcn3/32644.gcn3>
- Huang, Y. F., Wu, X. F., Dai, Z. G., Ma, H. T., & Lu, T. 2004, *ApJ*, 605, 300, doi: [10.1086/382202](https://doi.org/10.1086/382202)
- Huang, Y., Hu, S., . S. C. e. 2022, *LHAASO observed GRB 221009A with more than 5000 VHE photons up to around 18 TeV*. <https://gcn.gsfc.nasa.gov/gcn3/32677.gcn3>
- Isravel, H., Pe'er, A., & Begue, D. 2022, *arXiv e-prints*, arXiv:2210.02363, doi: [10.48550/arXiv.2210.02363](https://doi.org/10.48550/arXiv.2210.02363)
- Kann, D. A., Agayeva, S., Aivazyanyan, V., et al. 2023, *arXiv e-prints*, arXiv:2302.06225, doi: [10.48550/arXiv.2302.06225](https://doi.org/10.48550/arXiv.2302.06225)
- Kippen, R. M., Briggs, M. S., Kommers, J. M., et al. 1998, *ApJL*, 506, L27, doi: [10.1086/311634](https://doi.org/10.1086/311634)
- Klose, S., Schmidl, S., Kann, D. A., et al. 2019, *A&A*, 622, A138, doi: [10.1051/0004-6361/201832728](https://doi.org/10.1051/0004-6361/201832728)
- Knödlseeder, J. 2020, *arXiv preprint arXiv:2004.09213*
- Kraichnan, R. H. 1965, *Physics of Fluids*, 8, 1385, doi: [10.1063/1.1761412](https://doi.org/10.1063/1.1761412)
- Kuin, N. P. M., Dichiara, S., & Swift/UVOT Team. 2022, *GRB Coordinates Network*, 32656, 1
- Kumar, P., & Zhang, B. 2015, *PhR*, 561, 1, doi: [10.1016/j.physrep.2014.09.008](https://doi.org/10.1016/j.physrep.2014.09.008)
- Laskar, T., Berger, E., Margutti, R., et al. 2015, *ApJ*, 814, 1, doi: [10.1088/0004-637X/814/1/1](https://doi.org/10.1088/0004-637X/814/1/1)
- Laskar, T., Alexander, K. D., Margutti, R., et al. 2023a, *arXiv e-prints*, arXiv:2302.04388, doi: [10.48550/arXiv.2302.04388](https://doi.org/10.48550/arXiv.2302.04388)
- . 2023b, *ApJL*, 946, L23, doi: [10.3847/2041-8213/acbfad](https://doi.org/10.3847/2041-8213/acbfad)
- Lemoine, M., & Revenu, B. 2006, *MNRAS*, 366, 635, doi: [10.1111/j.1365-2966.2005.09912.x](https://doi.org/10.1111/j.1365-2966.2005.09912.x)
- Lesage, S., Veres, P., Roberts, O. J., et al. 2022, *GRB Coordinates Network*, 32642, 1
- Lesage, S., Veres, P., Briggs, M. S., et al. 2023, *arXiv e-prints*, arXiv:2303.14172, doi: [10.48550/arXiv.2303.14172](https://doi.org/10.48550/arXiv.2303.14172)
- LHAASO-Collaboration, Cao, Z., Aharonian, F., et al. 2023, *Science*, 0, eadg9328, doi: [10.1126/science.adg9328](https://doi.org/10.1126/science.adg9328)
- Lorenz, Eckartand Martinez, M. 2005, *Astronomy & Geophysics*, 46, 6.21, doi: [10.1111/j.1468-4004.2005.46621.x](https://doi.org/10.1111/j.1468-4004.2005.46621.x)
- MAGIC Collaboration, Acciari, V. A., Ansoldi, S., et al. 2019, *Nature*, 575, 455, doi: [10.1038/s41586-019-1750-x](https://doi.org/10.1038/s41586-019-1750-x)
- Medvedev, M. V. 2006, *ApJL*, 651, L9, doi: [10.1086/509075](https://doi.org/10.1086/509075)
- Medvedev, M. V., & Loeb, A. 1999, *ApJ*, 526, 697, doi: [10.1086/308038](https://doi.org/10.1086/308038)
- Mészáros, P. 2006, *Reports on Progress in Physics*, 69, 2259, doi: [10.1088/0034-4885/69/8/R01](https://doi.org/10.1088/0034-4885/69/8/R01)
- Mészáros, P., Rees, M. J., & Wijers, R. A. M. J. 1998, *ApJ*, 499, 301, doi: [10.1086/305635](https://doi.org/10.1086/305635)

- Miceli, D., & Nava, L. 2022, *Galaxies*, 10, 66, doi: [10.3390/galaxies10030066](https://doi.org/10.3390/galaxies10030066)
- Nava, L. 2018, *International Journal of Modern Physics D*, 27, 1842003, doi: [10.1142/S0218271818420038](https://doi.org/10.1142/S0218271818420038)
- Niemiec, J., Ostrowski, M., & Pohl, M. 2006, *ApJ*, 650, 1020, doi: [10.1086/506901](https://doi.org/10.1086/506901)
- O'Connor, B., Troja, E., Ryan, G., et al. 2023, arXiv e-prints, arXiv:2302.07906, doi: [10.48550/arXiv.2302.07906](https://doi.org/10.48550/arXiv.2302.07906)
- Omodei, N., bruel, P., . b. J. e. a. 2022a, GRB 221009A: Fermi LAT data rate effects due to extremely high flux. <https://gcn.gsfc.nasa.gov/gcn3/32760.gcn3>
- . 2022b, GRB 221009A: Extended Bad Time Intervals for Fermi LAT data. <https://gcn.gsfc.nasa.gov/gcn3/32916.gcn3>
- Paczynski, B. 1990, *ApJ*, 348, 485, doi: [10.1086/168257](https://doi.org/10.1086/168257)
- Paczynski, B., & Rhoads, J. E. 1993, *ApJL*, 418, L5, doi: [10.1086/187102](https://doi.org/10.1086/187102)
- Panaitescu, A., & Kumar, P. 2000, *ApJ*, 543, 66, doi: [10.1086/317090](https://doi.org/10.1086/317090)
- Pillera, R., Bissaldi, E., & Omodei, N., e. a. 2022, GRB 221009A: Fermi-LAT refined analysis. <https://gcn.gsfc.nasa.gov/gcn3/32658.gcn3>
- Piran, T. 1999, *PhR*, 314, 575, doi: [10.1016/S0370-1573\(98\)00127-6](https://doi.org/10.1016/S0370-1573(98)00127-6)
- Piran, T., Shemi, A., & Narayan, R. 1993, *Monthly Notices of the Royal Astronomical Society*, 263, 861, doi: [10.1093/mnras/263.4.861](https://doi.org/10.1093/mnras/263.4.861)
- Razzaque, S., Dermer, C. D., & Finke, J. D. 2010, *The Open Astronomy Journal*, 3, 150, doi: [10.2174/1874381101003010150](https://doi.org/10.2174/1874381101003010150)
- Ren, J., Wang, Y., & Zhang, L.-L. 2022, arXiv e-prints, arXiv:2210.10673, doi: [10.48550/arXiv.2210.10673](https://doi.org/10.48550/arXiv.2210.10673)
- Ressler, S. M., & Laskar, T. 2017, *ApJ*, 845, 150, doi: [10.3847/1538-4357/aa8268](https://doi.org/10.3847/1538-4357/aa8268)
- Reynolds, S. P., Williams, B. J., Borkowski, K. J., & Long, K. S. 2021, *ApJ*, 917, 55, doi: [10.3847/1538-4357/ac0ced](https://doi.org/10.3847/1538-4357/ac0ced)
- Rybicki, G. B., & Lightman, A. P. 1986, *Radiative Processes in Astrophysics* (Wiley-VCH)
- Salafia, O. S., Ravasio, M. E., Yang, J., et al. 2022, *ApJL*, 931, L19, doi: [10.3847/2041-8213/ac6c28](https://doi.org/10.3847/2041-8213/ac6c28)
- Sari, R., & Esin, A. A. 2001, *ApJ*, 548, 787, doi: [10.1086/319003](https://doi.org/10.1086/319003)
- Sari, R., & Piran, T. 1995, *ApJL*, 455, L143, doi: [10.1086/309835](https://doi.org/10.1086/309835)
- Sari, R., Piran, T., & Narayan, R. 1998, *The Astrophysical Journal*, 497, L17, doi: [10.1086/311269](https://doi.org/10.1086/311269)
- Sato, Y., Murase, K., Ohira, Y., & Yamazaki, R. 2023, *MNRAS*, 522, L56, doi: [10.1093/mnras/522.L56](https://doi.org/10.1093/mnras/522.L56)
- Schlegel, D. J., Finkbeiner, D. P., & Davis, M. 1998, *ApJ*, 500, 525, doi: [10.1086/305772](https://doi.org/10.1086/305772)
- Shrestha, M., Sand, D. J., Alexander, K. D., et al. 2023, *ApJL*, 946, L25, doi: [10.3847/2041-8213/acbd50](https://doi.org/10.3847/2041-8213/acbd50)
- Sironi, L., & Spitkovsky, A. 2011, *ApJ*, 726, 75, doi: [10.1088/0004-637X/726/2/75](https://doi.org/10.1088/0004-637X/726/2/75)
- Tan, W. J., Li, C. K., Ge, M. Y., et al. 2022, *The Astronomer's Telegram*, 15660, 1
- Totani, T. 1998, *ApJL*, 502, L13, doi: [10.1086/311489](https://doi.org/10.1086/311489)
- Veres, P., Burns, E., & Bissaldi, E., e. a. 2022, GRB 221009A: Fermi GBM detection of an extraordinarily bright GRB. <https://gcn.gsfc.nasa.gov/gcn3/32636.gcn3>
- Vietri, M. 1997, *Phys. Rev. Lett.*, 78, 4328, doi: [10.1103/PhysRevLett.78.4328](https://doi.org/10.1103/PhysRevLett.78.4328)
- Wang, X.-Y., Liu, R.-Y., Zhang, H.-M., Xi, S.-Q., & Zhang, B. 2019, *ApJ*, 884, 117, doi: [10.3847/1538-4357/ab426c](https://doi.org/10.3847/1538-4357/ab426c)
- Warren, D. C., Barkov, M. V., Ito, H., Nagataki, S., & Laskar, T. 2018, *MNRAS*, 480, 4060, doi: [10.1093/mnras/sty2138](https://doi.org/10.1093/mnras/sty2138)
- Waxman, E., & Bahcall, J. N. 2000, *ApJ*, 541, 707, doi: [10.1086/309462](https://doi.org/10.1086/309462)
- Williams, M. A., Kennea, J. A., Dichiara, S., et al. 2023, *ApJL*, 946, L24, doi: [10.3847/2041-8213/acbcd1](https://doi.org/10.3847/2041-8213/acbcd1)
- Woosley, S. E., Heger, A., & Weaver, T. A. 2002, *Reviews of Modern Physics*, 74, 1015, doi: [10.1103/RevModPhys.74.1015](https://doi.org/10.1103/RevModPhys.74.1015)
- Wright, E. L. 2006, *PASP*, 118, 1711, doi: [10.1086/510102](https://doi.org/10.1086/510102)
- Yamasaki, S., & Piran, T. 2022, *MNRAS*, 512, 2142, doi: [10.1093/mnras/stac483](https://doi.org/10.1093/mnras/stac483)
- Zhang, B. 2018, *The Physics of Gamma-Ray Bursts* (Cambridge University Press), doi: [10.1017/9781139226530](https://doi.org/10.1017/9781139226530)
- Zhang, B., & Mészáros, P. 2001, *ApJ*, 559, 110, doi: [10.1086/322400](https://doi.org/10.1086/322400)
- Zhang, B., Liang, E., Page, K. L., et al. 2007, *ApJ*, 655, 989, doi: [10.1086/510110](https://doi.org/10.1086/510110)
- Zhang, B. T., Murase, K., Ioka, K., et al. 2022, arXiv e-prints, arXiv:2211.05754, doi: [10.48550/arXiv.2211.05754](https://doi.org/10.48550/arXiv.2211.05754)
- Zhang, B. T., Murase, K., Kimura, S. S., Horiuchi, S., & Mészáros, P. 2018, *PhRvD*, 97, 083010, doi: [10.1103/PhysRevD.97.083010](https://doi.org/10.1103/PhysRevD.97.083010)